Novel high-entropy perovskite $Ba(Zn_{0.2}Yb_{0.2}Ta_{0.2}Nb_{0.2}V_{0.2})O_3$ ceramic with excellent electromagnetic wave absorption properties

Henghai Zhu[a,b], Yingbiao Peng[a*], Han Chen[b], Yang Li[c], Wei Zhou[b*]

[a] College of Materials and Advanced Manufacturing, Hunan University of Technology, Zhuzhou 412007, China

[b] Hunan Key Laboratory of Applied Environmental Photocatalysis, Changsha University, Changsha, 410022, China

[c] State Key Laboratory of Powder Metallurgy, Central South University, Changsha, 410083, China

Abstract:

To solve the increasingly serious problem of electromagnetic wave (EW) pollution, a development procedure for high-performance EW absorption (EWA) materials is urgently required. High-entropy ceramics offer a good prospect in the field of EWA materials due to their unique effect brought by multi-component elements. Therefore, in this study, the composition of high-entropy ceramics was designed by utilizing the Goldschmidt tolerance factor. Then, the high-entropy perovskite $Ba(Zn_{0.2}Yb_{0.2}Ta_{0.2}Nb_{0.2}V_{0.2})O_3$ (BZO) ceramic with high EWA performance was prepared by high-temperature solid-phase method. The EWA mechanism of the material was explored based on the phase composition, microstructure, and electromagnetic parameters of the specimens. Good impedance matching and better

* Corresponding author. E-mail address: pengyingbiao1987@163.com (Y. Peng), zhouwei_csu@163.com (W. Zhou).

attenuation ability were obtained for BZO sintered at 1100 °C (BZO-1100) due to the crystallographic transition and increase in crystal interfaces. Consequently, BZO-1100 achieved excellent EWA performance at a thickness of 2.12 mm, with a minimum reflection loss of −54.09 dB and an effective absorption bandwidth of 2.81 GHz in the X-band. Moreover, the possibility of the practical application of BZO high-entropy ceramics was verified by electric field distribution simulations and radar cross section simulations. This study provides a valuable reference for the design of high-performance high-entropy perovskite ceramic EWA materials.

Keywords: Perovskite; High-entropy ceramics; Electromagnetic wave absorption; Radar cross section simulation

1. Introduction

With the rapid advancement of fifth-generation communication technologies and electronic devices, proliferation of electromagnetic waves (EWs) emitted from various sources represents a significant hazard to both human health and equipment integrity [1, 2]. Therefore, the investigation of efficient EW absorption (EWA) materials has attracted significant research interest at the global scale. However, due to the miniaturization of electronic devices and complex application environments, EWA materials need to simultaneously exhibit high absorption, wide bandwidth, thin thickness, and light weight [3, 4]. To meet the above-mentioned requirements, a large pool of potential candidates for EWA materials has emerged, which includes carbon-based absorbents [4–7], silicon-based absorbents [8, 9], rare-earth metallic

compounds [10–12], ceramic materials [13–15], MXenes [16, 17], metal–organic frameworks [18, 19], and transition metal oxides [20-22]. Among these materials, high-entropy ceramics have been considered as one of the ideal EWA materials in the last decade due to their unique physical and chemical properties [23].

The concept of high-entropy ceramics is derived from the term “high-entropy alloys” (HEAs) [24]. Similar to HEAs, high-entropy ceramics are usually defined as solid solutions with high conformational entropy, and they are composed of five (or more) cationic or anionic subcrystals with an atomic concentration of 5–35% [25]. In 2015, Rost et al. highlighted the concept of high-entropy ceramics for the first time by successfully preparing high-entropy oxide ceramics with rock salt structure [26]. They not only applied the concept of high-entropy in the field of ceramics, but also brought high-entropy ceramics to the attention of researchers. Subsequently, a wide variety of high-entropy ceramics has sprung up in numerous fields, such as thermal barrier coatings [27], photocatalysis [28], lithium-ion batteries [29], anti-oxidation coatings [30], EWA materials [31, 32], etc. The utilization of high-entropy ceramics in various significant fields can be attributed to their unique set of four effects: (i) High entropy effect, (ii) Lattice distortion effect, (iii) Sluggish diffusion effect, and (iv) Cocktail effect. The four primary effects of high-entropy ceramics on EWA materials derived from these ceramics can be succinctly summarized as follows [33]. The high-entropy effect facilitates the formation of a stable solid solution at high temperatures and aids in maintaining the crystal structure of the material. The lattice distortion effect refers to the lattice distortion caused by different crystal structures and bond energies

between the constituent elements, which results in defect generation. In contrast, the sluggish diffusion effect induces grain boundary dislocations and non-uniform diffusion of grains, enhancing the local structural stability of the material. This phenomenon contributes to the enhancement of the oxidation and corrosion resistance of the material, as well as its mechanical strength. The cocktail effect refers to the interactions among components with different properties in high-entropy ceramics, which enables high-entropy ceramics to simultaneously exhibit complex and diverse properties of different components. High-entropy ceramic materials with outstanding EWA properties can be acquired by utilizing the four primary effects in component design [34].

Perovskite oxides (ABO_3) have been applied in many practical fields such as energy storage, catalysis, and EWA due to their excellent structural stability, low density, wide band gap, and good catalytic properties [35, 36]. Interestingly, the stable perovskite oxide consists of an A-site cation with coordination number 12, a B-site cation with coordination number 6, and an octahedral oxygen anion. Incorporation of multiple metal cations with different properties makes it feasible to attain the desired coordination number of A-site/B-site cations that can meet the specified conditions. This presents a crucial avenue for designing and tuning the properties of high-entropy perovskite oxides. Noteworthy, Goldschmidt tolerance factor (t_G) is one of the efficient judgments for predicting the stability when designing high-entropy perovskite oxides, and is calculated as follows [37]:

$$t_G = \frac{R_A + R_O}{\sqrt{2}(R_B + R_O)} \quad (1)$$

where R_A, R_B, and R_O represent the average ionic radii of the A-site cation, B-site cation, and oxygen anion, respectively. When $0.75 \leq t_G \leq 1$, a stable perovskite structure is maintained in the high-entropy ceramics. Specifically, $0.9 \leq t_G \leq 1$ forms a cubic phase; when $t > 1.0$, a tetragonal or hexagonal phase may be formed; and for $0.75 \leq t_G < 0.9$, an orthorhombic or rhombic phase may be formed.

To achieve the stable formation of novel high-entropy ceramics with perovskite-type structures, Ba^{2+} ions were specifically used for the A-site. Next, the combination of metal elements in the B-site was designed herein, and the corresponding t_G was calculated. First, V, Nb, and Ta, all belonging to the VI B group with similar chemical properties, were selected. Subsequently, elements Zn and Yb were selected for valence and coordination number considerations. The t_G of $Ba(Zn_{0.2}Yb_{0.2}Ta_{0.2}Nb_{0.2}V_{0.2})O_3$ was calculated to be 1.00. Therefore, the specimen was expected to form a stable perovskite structure.

In this study, $Ba(Zn_{0.2}Yb_{0.2}Ta_{0.2}Nb_{0.2}V_{0.2})O_3$ (BZO) high-entropy ceramics were prepared by a high-temperature solid-phase method. The phase composition, microstructure, and EWA properties were systematically investigated. Furthermore, the electric field distribution and radar cross section (RCS) properties were simulated and calculated to reveal the EWA mechanism of the materials. This study provides a useful literature reference for the development and application of ABO_3 type high-entropy oxide ceramics in EWA.

2. Experimental

2.1. Specimens Preparation

All the reagents utilized in the preparation were of analytical grade. $BaCO_3$, ZnO, Yb_2O_3, Nb_2O_5, Ta_2O_5, and V_2O_5 powders were mixed according to the metal ion molar ratio of 5:1:1:1:1:1:1. Next, to the resulting mixed powder, appropriate amount of anhydrous ethanol was added and then the mixture was ball milled at 300 $r \cdot min^{-1}$ for 20 h. The mixture was transferred to an oven for drying at 60 °C for 24 h. Dried powder was sieved to produce the precursor. After adding an appropriate amount of polyvinyl alcohol (PVA), the precursor was cold pressed in a mold with a diameter of 50 mm. The relevant cold pressing pressure was 10 MPa and the holding time was 1 min. Finally, the pressed powder discs were transferred to a muffle furnace for sintering. The furnace was slowly heated to 550 °C at 1 $°C \cdot min^{-1}$ for PVA exclusion, and then ramped up to the target sintering temperature (1000–1400 °C) at 5 $°C \cdot min^{-1}$. According to the target sintering temperature, the five specimens were named as BZO-1000, BZO-1100, BZO-1200, BZO-1300, and BZO-1400, respectively. The fabrication process of BZO high-entropy ceramics is schematically shown in Fig. 1.

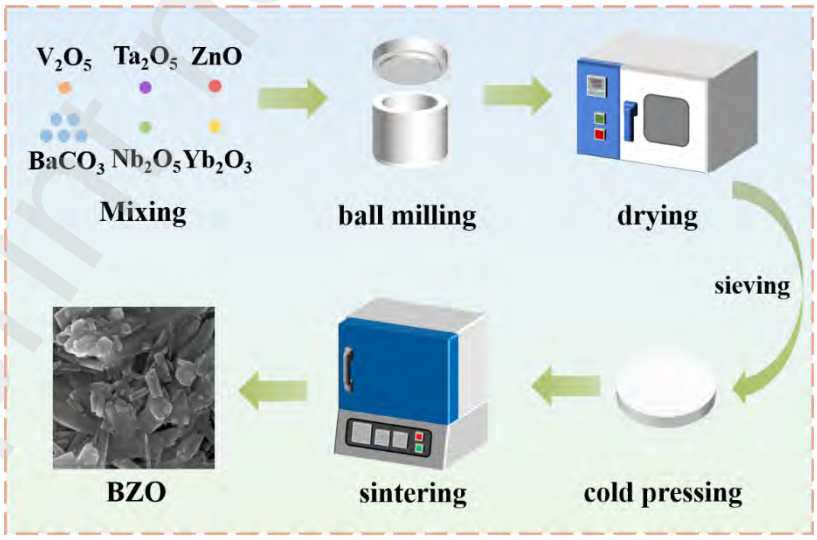

Fig. 1 The fabrication process of BZO high-entropy ceramics.

2.2. Characterization

The phase composition of BZO was analyzed by X-ray diffraction (XRD, Ultima IV, Rigaku). The morphology and elemental distribution of the prepared specimens were characterized by scanning electron microscopy (SEM, JEM-6700F, JEOL) and transmission electron microscopy (TEM, JEM-3010F, JEOL). The permittivity and permeability in the frequency range of X-band (8.2–12.4 GHz) were measured by the waveguide method through a vector network analyzer (N5230A, Agilent). The sintered specimens were cut into rectangular shape with a length of 22.89 mm, a width of 10.18 mm, and a thickness of 2 mm**.** The electric field distribution and RCS were simulated by using ANSYS Electronics Desktop software. In order to facilitate calculations, the simulation model of the specimens was simplified. The electric field distribution model size was 22.89 μm × 10.18 μm × 2 μm and the RCS model size was 180 mm × 180 mm × 3 mm.

3. Results and discussion

3.1. Microstructural characteristics and phase component

Fig. 2a shows the XRD patterns of BZO specimens obtained at different temperatures. At lower temperatures (1000–1100 °C), the XRD patterns of the specimens were consistent and the individual diffraction peaks could correspond to the PDF cards of the perovskite oxides. With the increase in temperature, the singular diffraction peak of the specimen commenced to decompose into multiple peaks, concomitant with a diminution in the peak intensities. When a temperature threshold of 1400 °C was reached, the diffraction peak intensities attenuated to such an extent that it became challenging to discern them in contrast to observations at lower

temperatures. The alteration observed in the XRD pattern indicates a potential transformation in the crystallographic and phase architecture of the material.

To advance the analysis of the phase structural alterations in the material, SEM investigation was conducted on the specimens subjected to various thermal conditions (as depicted in Figs. 2b–f). At a temperature of 1000 °C, the specimen exhibits a morphology characterized by substantial particulate structures. With the increase in the temperature to 1100 °C, the formation of columnar crystallites initiates in the material, albeit in concert with a residual presence of particulates (denoted by red circular marks). With the further thermal increment, the specimen initially coalesces into large aggregates of columnar crystals (as depicted in Fig. 2d), subsequently transitioning into a dispersion of diminutive columnar crystallites with diverse morphologies (illustrated in Fig. 2e). Finally, at a temperature of 1400 °C, the formation of columnar crystals culminates, and the material exhibits a uniform morphological profile (shown in Fig. 2f). Changes in crystal structure introduce a wealth of interfaces and defects in the material, which results in the increased polarization relaxation. Furthermore, the observed alterations in the crystalline structure are in concordance with the analytical insights derived from XRD pattern. The XRD profiles underwent a transition from acute and symmetric peaks to diminished and diffused peaks with asymmetric contours, as the specimens evolved from large-size particulate forms to small-size columnar crystallites. Fig. 3 illustrates the TEM micrographs of the BZO-1100 and BZO-1200 specimens. The images reveal that the specimens processed at 1200 °C retain particulate features, yet the dimensions

of these particles are markedly reduced relative to the specimen subjected to the treatment at 1100 °C. This observation infers the presence of a small number of particles that have not been converted into columnar crystals, indicating an incomplete phase transition at the elevated temperature of 1200 °C. This conclusion is consistent with the SEM analysis results. Furthermore, elemental mapping analysis confirms uniform distribution of constituent elements throughout the material. Synergistic integration of the findings of XRD, SEM, and TEM analyses evidently indicates the successful synthesis of the high-entropy perovskite ceramic BZO.

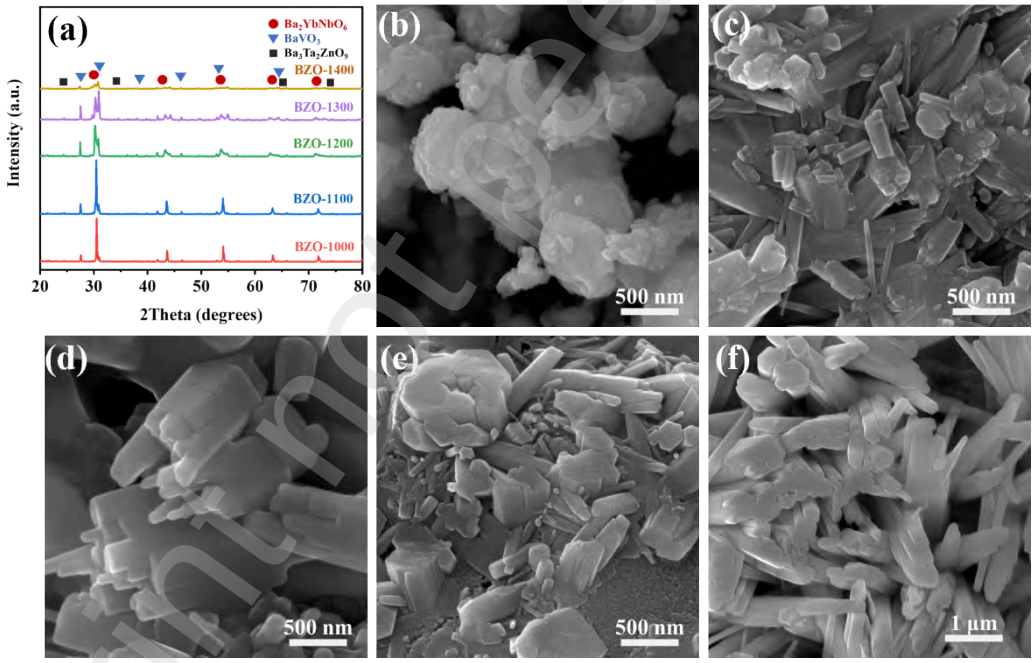

Fig. 2 (a) XRD patterns of BZO specimens; and SEM images of BZO specimens: (b) BZO-1000, (c) BZO-1100, (d) BZO-1200, (e) BZO-1300, and (f) BZO-1400.

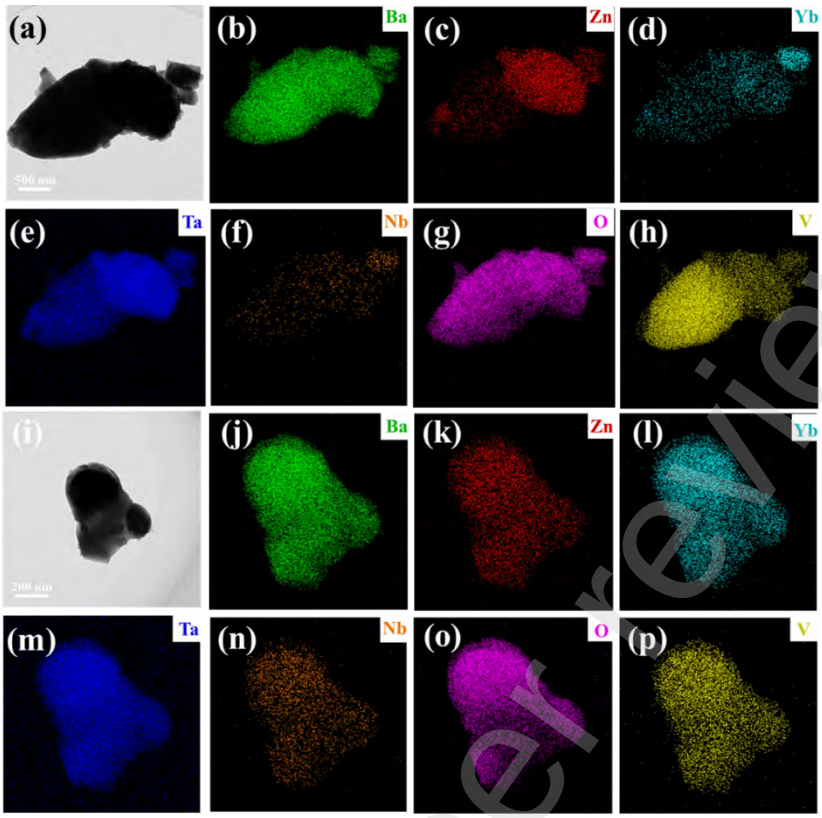

Fig. 3 TEM images of (a) BZO-1100 and (b–h) corresponding mapping; (i) TEM images of BZO-1200 and (j–p) corresponding mapping.

3.2. EWA property

In accordance with transmission line theory, the EWA performance of specimens can be quantitatively assessed by determining the minimum reflection loss (RL_{min}). This critical parameter can be derived by applying the following mathematical formulas [38, 39]:

$$RL = 20 \lg \left| \frac{Z_{in} - Z_0}{Z_{in} + Z_0} \right| \quad (2)$$

$$Z_{in} = Z_0 \sqrt{\frac{\mu_r}{\varepsilon_r}} \tanh\left(j \frac{2\pi f d}{c} \sqrt{\mu_r \varepsilon_r} \right) \quad (3)$$

where Z_{in} and Z_0 represent the input impedance and characteristic impedance of air, respectively. ε_r and μ_r (BZO has no magnetic component, the corresponding μ_r is considered as 1) are the relative complex permittivity and permeability, respectively.

c refers to the velocity of light, f denotes the frequency of electromagnetic waves, and d represents thickness of specimens. Fig. 4 shows the RL values and impedance matching of BZO ceramics in the X-band. Figs. 4a–f illustrate that the BZO specimens exhibit suboptimal EWA characteristics at increased thicknesses, whereas they demonstrate enhanced EWA efficacy in the thinner range of 1.0–2.4 mm. To facilitate a more explicit comparison of the EWA capabilities of BZO specimens across varying temperatures, the RL_{min} values were obtained alongside their corresponding effective absorption bandwidth (EAB) for specimens with different thicknesses, as illustrated in Figs. 4a1–f1. It is observed that the BZO-1100, BZO-1200, and BZO-1300 specimens exhibit commendable EWA properties. Notably, the BZO-1100 specimen stands out with the most favorable RL_{min} value of −54.09 dB at 9.4 GHz, coupled with an extensive EAB of 2.81 GHz. The EWA performance of BZO specimen can be preliminarily explained in terms of impedance matching (as shown in Figs. 4a2–e2). At thinner thicknesses, BZO-1100, BZO-1200, and BZO-1300 specimens exhibit a greater number of regions where the impedance matching approaches an ideal value of 1. In contrast, the BZO-1000 and BZO-1400 specimens exhibit a limited number of impedance matching regions, which conduces to their relatively inferior EWA performance. Furthermore, Fig. 5 presents a comparative evaluation of the BZO specimens against other recently documented EWA materials. The data presented in Table 1 complement this analysis by providing the pertinent thicknesses of the compared materials. The data reveal that, in contrast to these EWA materials, the BZO-1100 boasts superior EWA characteristics at lower thicknesses.

This result suggests that the BZO specimen stands out as a promising candidate for an efficacious EWA material.

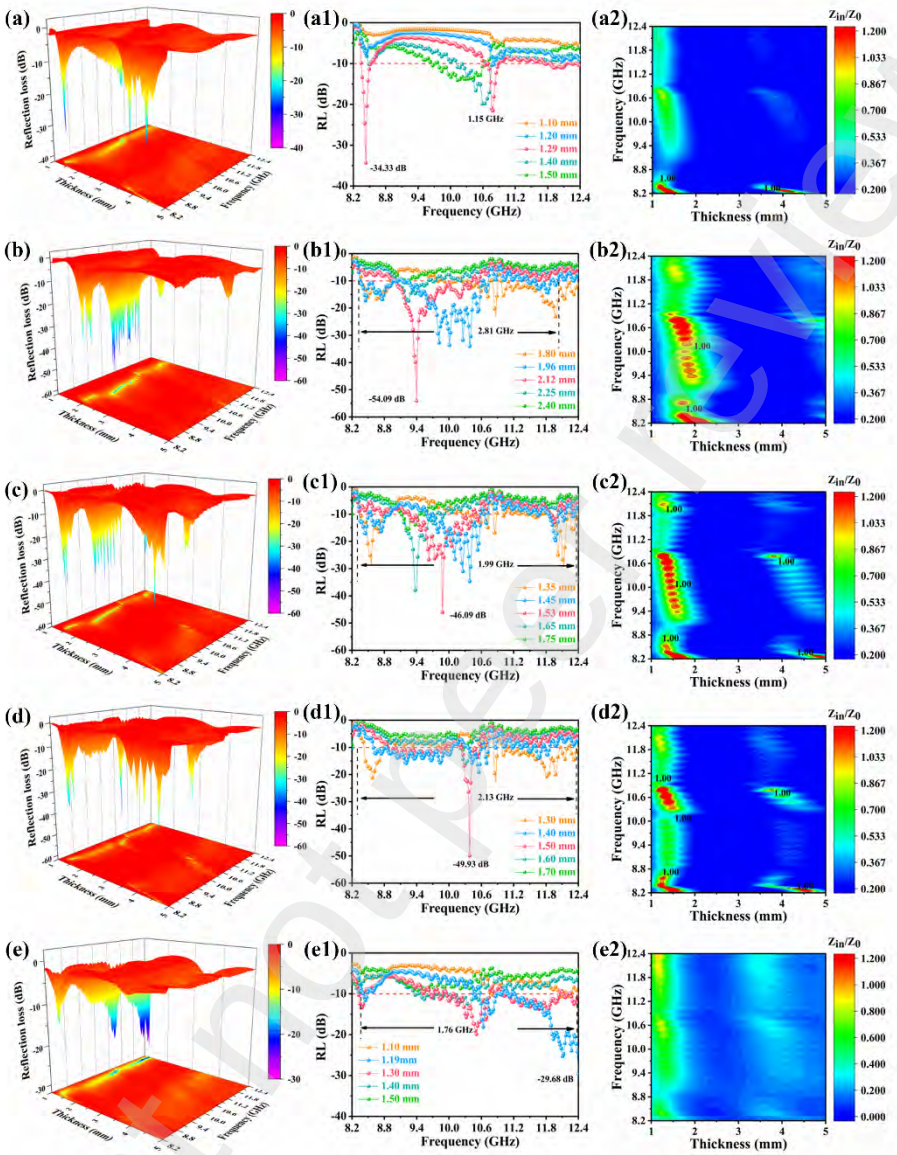

Fig. 4 (a–e) The 3D RL values of BZO specimens; (a1–e1) RL values of BZO specimens at different thicknesses and (a2–e2) the Z_{in}/Z_0 of BZO specimens.

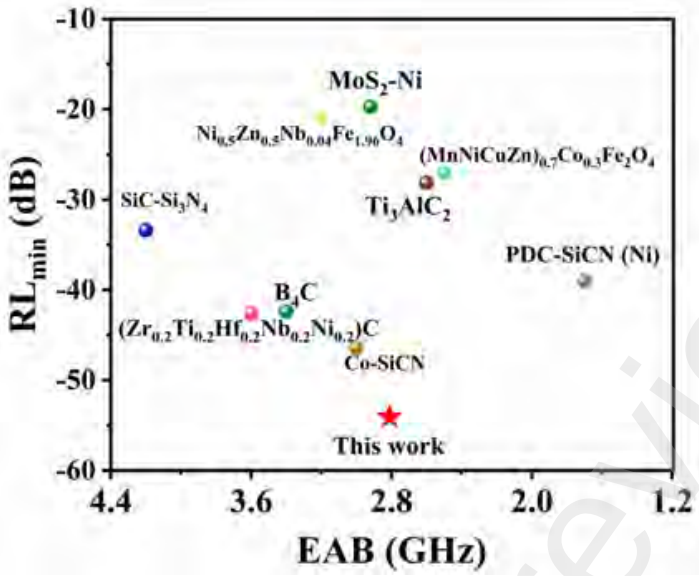

Fig. 5 Comparison of EWA performance of BZO with other EWA materials.

Table 1. EWA performance of BZO and other reported materials.

Materials	RL_{min} (−dB)	EAB (GHz)	Thickness (mm)	Ref.
B_4C	−42.42	3.4	2.9	[40]
MoS_2-Ni	−19.7	2.92	4.8	[41]
Ti_3AlC_2	−28.11	2.6	3.13	[42]
SiC-Si_3N_4	−33.4	4.2	3	[43]
PDC-SiCN (Ni)	−39	1.7	2	[44]
Co-SiCN	−46.4	3	1.05	[45]
$(MnNiCuZn)_{0.7}Co_{0.3}Fe_2O_4$	−27	2.5	5.3	[46]
$Ni_{0.5}Zn_{0.5}Nb_{0.04}Fe_{1.96}O_4$	−20.8	3.2	8.5	[47]
$(Zr_{0.2}Ti_{0.2}Hf_{0.2}Nb_{0.2}Ni_{0.2})C$	−42.61	3.6	1	[48]
BZO	−54.09	2.81	2.12	This study

3.3. EWA mechanism

For further systematic investigation of the fundamental factors affecting the EWA characteristics of the as-prepared specimens, a thorough investigation on the dielectric properties was conducted. According to Debye theory, the real part (ε') and imaginary part (ε") corresponding to the storage capacity and attenuation ability, respectively, can be represented by the following equations [49, 50]:

$$\varepsilon' = \varepsilon_\infty + \frac{\varepsilon_s - \varepsilon_\infty}{1 + \omega^2\tau^2} \quad (4)$$

$$\varepsilon'' = \frac{\varepsilon_s - \varepsilon_\infty}{1 + \omega^2\tau^2}\omega\tau + \frac{\sigma}{\omega\varepsilon_0} = \varepsilon_p'' + \varepsilon_c'' \quad (5)$$

where ε_0 denotes the vacuum permittivity, quantified as 8.854×10^{-12} $F \cdot m^{-1}$, ε_s signifies the static permittivity, and ε_∞ corresponds to the relative permittivity at light frequencies. The symbols σ, τ, and ω represent electrical conductivity, polarization relaxation time, and angular frequency, respectively. εp" and εc" refer to the contributions of the ε", arising from polarization loss and conductance loss. Fig. 6a shows the real part of the dielectric constant of different BZO specimens, which first decreases and then increases with increasing temperature. This fluctuation may be related to the polarization process and crystal structure. In general, high temperatures and centrosymmetric crystal structures result in low real parts of the dielectric constant. In case of BZO-1000, an elevated real part of the dielectric constant is observed, which can be attributed to its comparatively lower sintering temperature and prevalence of symmetric granular crystallites. With the increase in the temperature to 1100 °C, the specimen exhibits a coexistence of granular and columnar crystalline morphologies, leading to the formation of an asymmetric crystal structure. This morphological transition well correlates with a notable reduction in the dielectric constant of BZO-1100, reflecting the influence of crystal symmetry on the dielectric properties of the material. However, the concurrent existence of particulate and columnar crystalline forms in BZO-1000 introduces a plethora of structural defects and interfaces, which sustains the real part of the dielectric constant at a not too low

value. With the further increase in temperature, a substantial portion of the specimen undergoes a transformation into centrosymmetric columnar crystallites. This morphological evolution is accompanied by an increase in the dielectric constant, which also represents an increase in the attenuation of EWs. Fig. 6b exhibits that the imaginary part of the BZO specimen first decreases and then increases with temperature, which is related to the change in material conductivity and crystal structure. With the transition of the BZO high-entropy ceramics from granular to columnar crystalline forms, interconnected conductive pathways are established, which results in an enhancement in the imaginary component of the dielectric permittivity. Conversely, the observed decrease in the imaginary part of dielectric constant for BZO-1100 may be attributed to the thermal molecular movement, which disrupts the dipole orientational polarization of the molecular ensemble. This disruption leads to a reduction in the overall polarization capacity, as the contribution from defect-induced polarization is insufficient to counterbalance the loss of molecular dipole alignment. However, an excessively high imaginary part of the dielectric constant may cause an impedance mismatch, resulting in the reflection of more EWs, which do not enter the interior of the material. The dissipative capacity of a material with respect to EWs can be characterized by tan δ (tan $\delta = \varepsilon''/\varepsilon'$). An increased value of tan δ is indicative of the enhanced capability of the material to dissipate the energy of EWs. This parameter is intrinsically linked to the dielectric properties of the material and reflects its efficiency in converting electromagnetic energy into thermal energy, which is a manifestation of energy loss within the

material. Fig. 6c delineates that the specimens BZO-1000 and BZO-1400 exhibit higher values of tan δ at lower frequencies, implying a more pronounced energy dissipation capability compared to the other specimens. This observation indicates that BZO-1000 and BZO-1400 may offer superior loss characteristics under low-frequency conditions. However, the magnitudes of both the dielectric constant and tan δ represent but a single facet of the EWA performance. A comprehensive evaluation of EWA performance necessitates an integrated analysis, considering additional material properties and characteristics.

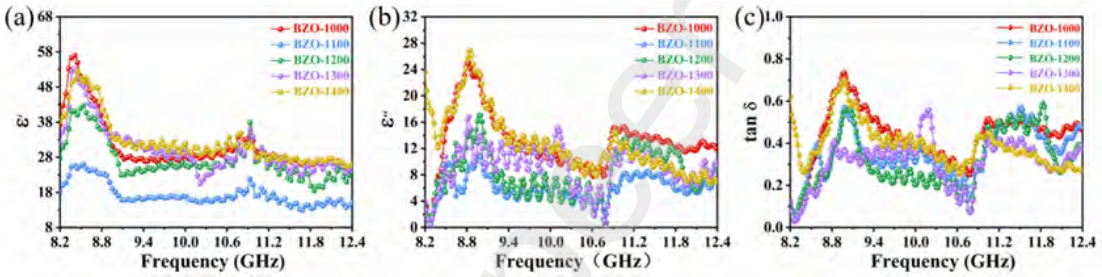

Fig. 6 (a) ε', (b) ε'', and (c) tan δ of BZO specimens.

Figs. 7a–e display the Cole–Cole diagrams for the BZO specimens, and these Cole–Cole curves are as irregular as those of some of the reported high-entropy materials [48, 51, 52]. Typically, a semicircular profile within a Cole–Cole plot indicates the occurrence of a unique Debye relaxation process, suggesting the mechanism of dielectric relaxation within the material. All BZO specimens demonstrate the presence of multiple Cole–Cole semicircular features, confirming the existence of concurrent dielectric relaxation processes within the BZO matrix. Furthermore, the Cole–Cole plots for BZO high-entropy ceramics exhibit short or negligible tail extensions, implying that the polarization dissipation constitutes the predominant loss mechanism, significantly overshadowing the dielectric losses within the material. For high-entropy

materials, the presence of multi elements with different ionic radii tends to change the distribution of their influencing charges and promotes the formation of electric dipoles, which results in complex dipole polarization relaxation. Moreover, a variety of local defects such as defects, vacancies, lattice distortions, and grain boundaries, which are abundant in high-entropy ceramics, can also act as polarization centers, thus improving polarization relaxation and enhancing EWA performance.

Noteworthy, the electrical conductivity of a composite material is a pivotal parameter influencing its conductive loss behavior, which can be quantitatively assessed through the following formula [53]:

$$\sigma = 2\pi f \varepsilon_0 \varepsilon'' \quad (6)$$

Fig. 7f illustrates the change in conductivity of BZO high-entropy ceramics at different temperatures, revealing a non-monotonic trend wherein the conductivity initially diminishes and subsequently escalates with the augmentation of temperature. This behavior is consistent with the change in the imaginary part of the dielectric constant, caused by the transformation of the crystal shape and accelerated motion of electrons at high temperatures. In general, a larger conductivity represents a larger conduction loss. However, the increase in conductivity also indicates that more EWs are reflected by the material, leading to a decrease in the impedance matching performance of BZO-1000 and BZO-1400 and a decrease in EWA efficiency.

The input impedance serves as a direct indicator of the efficacy of impedance matching between a material and the incident EWs, with optimal matching being attained when the input impedance of the material is infinitely close to the free-space

impedance (Z_0, 377 Ω) [54]. This condition ensures minimal reflection and maximal absorption of the electromagnetic energy, which is essential for designing materials for EWA applications. Fig. 8a presents the input impedance characteristics of the BZO specimens subjected to different temperature, where the input impedance of the all BZO specimens is lower than the Z_0 value. The low input impedance is caused by the excessively high imaginary part of the dielectric constant of the BZO specimens. Among the specimens, BZO-1100 stands out with a significantly higher input impedance, indicating that it exhibits best impedance matching properties. This enhanced impedance matching is indicative of a more effective absorption of the incident EWs, thereby reducing RL values and optimizing the EWA performance of the material.

The attenuation constant (α), a critical parameter in the assessment of the capacity of a material to diminish the intensity of EWs, is quantified through the following relationship [55]:

$$\alpha = \frac{\sqrt{2}\pi f}{c}\sqrt{\mu''\varepsilon'' - \mu'\varepsilon' + \sqrt{\left(\mu'^2 + \mu''^2\right)\left(\varepsilon'^2 + \varepsilon''^2\right)}} \quad (7)$$

A higher value of α indicates a greater ability to attenuate the EWs, which is desirable for applications requiring efficient EWA characteristic. Fig. 8b depicts the variation of α of BZO specimens at different temperatures, revealing a trend where the α initially decreases and subsequently escalates with an increase in temperature. This pattern is consistent with the variations observed in the dielectric constant. The BZO-1000 and BZO-1400 specimens exhibit increased attenuation constants, indicating their potential to effectively dissipate EW energy. However, their suboptimal

impedance matching impedes their EWA performance, as the inability to match the impedance of the material with that of the incident waves leads to increased reflection and reduced absorption. In contrast, the BZO-1200 and BZO-1300 specimens demonstrate intermediate levels of impedance matching and attenuation constants. Their enhanced EWA performance is attributed to the occurrence of a greater number of polarization relaxation processes, which facilitate more efficient energy dissipation mechanisms compared to the BZO-1000 and BZO-1400 variants. The BZO-1100 stands out among the high-entropy BZO ceramic specimens due to its optimal impedance matching, which is crucial for minimizing RL values and maximizing energy absorption. Coupled with favorable decay constants and a multiplicity of polarization relaxation processes, BZO-1100 exhibits the most effective EWA performance, making it a promising candidate for applications requiring superior EW management capabilities.

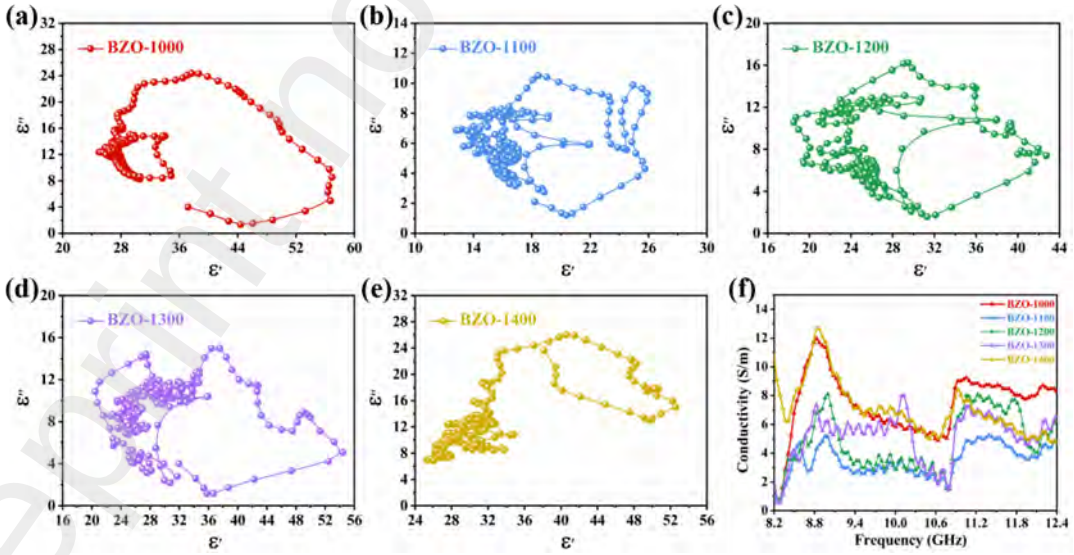

Fig. 7 (a–e) Cole–Cole plots and (f) conductivity of BZO specimens at different temperatures.

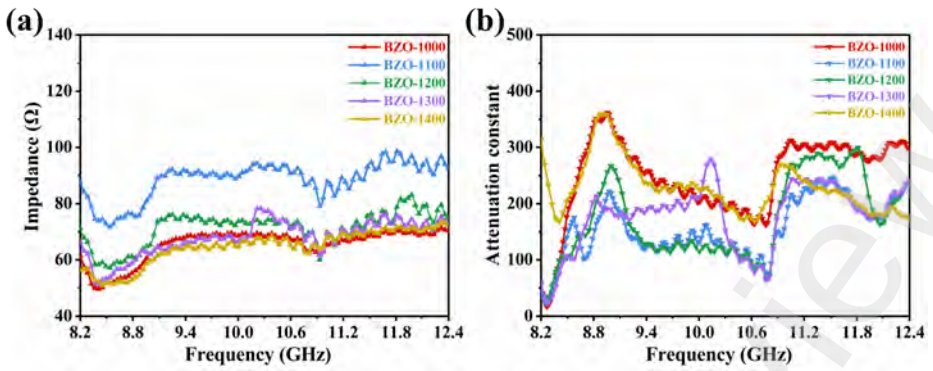

Fig. 8 The (a) Z_{in} value and (b) α value of BZO specimens.

Based on the above-mentioned analysis, the potential EWA mechanism of BZO high-entropy ceramics was determined, as shown in Fig. 9. With excellent impedance matching, most of the incident waves propagated into the prepared specimen with the reflection of only a very small portion. The columnar crystals formed by the high-entropy ceramics contacted each other and formed a conductive network, which increased the conductive loss. The contact of the columnar crystals with granular crystals introduced defects and heterogeneous interfaces, leading to significant interfacial polarization losses. Moreover, high entropy ceramics with multi-component metal ions generated dipole polarization between them, thus further optimizing the EWA performance. In summary, the superior EWA performance exhibited by $Ba(Zn_{0.2}Yb_{0.2}Ta_{0.2}Nb_{0.2}V_{0.2})O_3$ high-entropy ceramics could be attributed to the synergistic effects of optimal impedance matching and a multitude of effective attenuation mechanisms.

3.4. Electric field distribution and RCS simulation

For in-depth analysis of the EWA mechanism, the electric field distribution of a BZO high-entropy ceramic specimen was simulated by using ANSYS Electronics

Desktop software. To simplify the calculation, the size of the high-entropy ceramic specimen was reduced to 1/10 (22.89 μm × 10.18 μm × 2 μm). Fig. 10 shows the simulation results of the electric field distribution of BZO at different temperatures, where the electric field of BZO specimens first increases and then decreases with the increase in temperature. The maximum electric field strength was achieved with BZO-1100 (shown with more orange areas), while the lowest electric field strength was obtained for BZO-1000 and BZO-1400 (shown as mostly green areas). The highest electric field strength of the BZO-1100 was attributed to optimal impedance matching performance, resulting in more EWs entering the material rather than being reflected. Although BZO-1100 exhibits a lower conductivity than the other specimens, more EW waves entering the interior of the material endow it with the ability to generate more conduction current. Therefore, BZO-1100 shows the largest electric field strength, indicating that its actual conduction loss is the best among the BZO specimens. Moreover, this simulation result also shows that the conduction loss performance of EWA materials does not only depend on the dielectric constant imaginary part and conductivity, but on the combination of multiple factors such as dielectric constant imaginary part and impedance matching.

The RCS is a physical quantity that measures the ability of a target object to reflect radar waves, which can be used as one of the bases for judging the EWA performance for practical applications [56]. Therefore, the RCS performance of the materials at 9.4 GHz was calculated by simulation through ANSYS Electronics Desktop software. Figs. 11a–f demonstrate that the 3D RCS appearance of the BZO specimen is slightly

smaller than that of a perfect electrical conductor (PEC). Moreover, the color of the edges in the RCS plots of PEC is closer to red, while the color of the center in the BZO specimens is closer to blue. All these observations indicate that the RCS performance of the BZO specimens is better than that of the PEC, with BZO-1100 exhibiting the best performance. For visual comparative analysis, the RCS values of BZO-1100 and PEC are shown in Fig. 11g (Phi = 0°, Theta = 0–360°). When theta is 329°, a very small value of −32.74 dBm is achieved. At this point, the RCS of the BZO-1000 is reduced by 94.8% compared to that of the PEC, indicating the excellent RCS performance of the BZO-1100. This simulation is consistent with the EWA performance of BZO high-entropy ceramics.

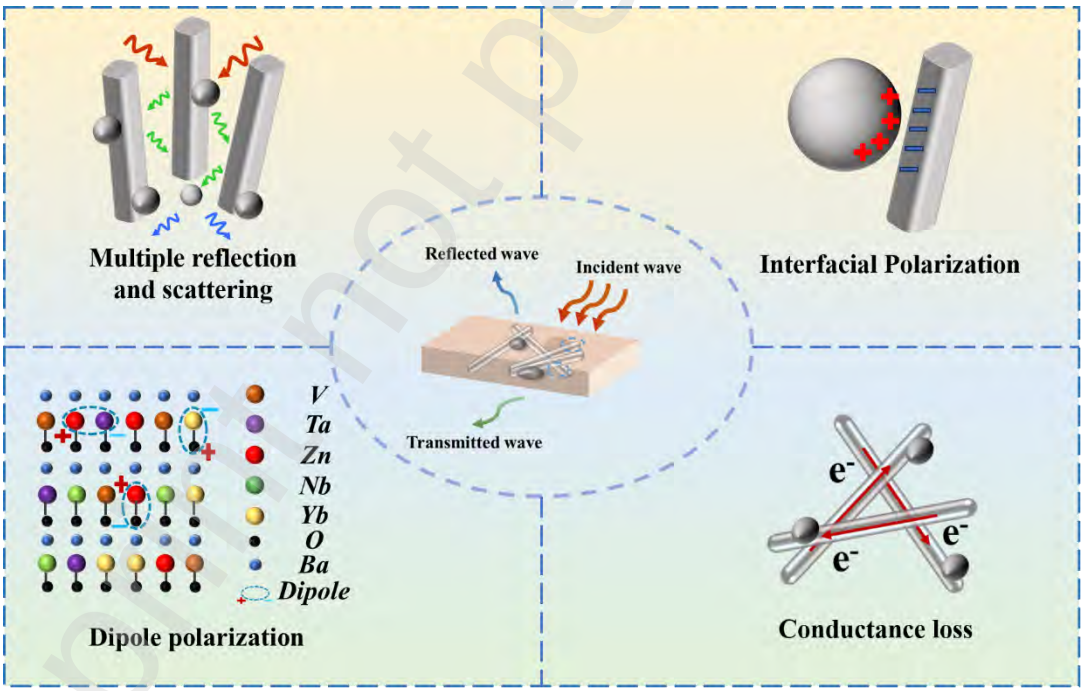

Fig. 9 Schematic illustration of the EWA mechanism of BZO high-entropy ceramics.

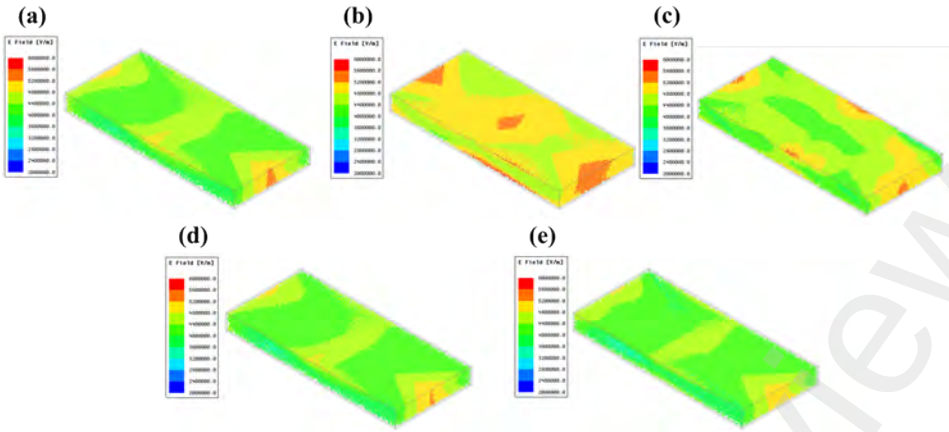

Fig. 10 Simulation results of electric field distribution in BZO high-entropy ceramics: (a) BZO-1000, (b) BZO-1100, (c) BZO-1200, (d) BZO-1300, and (e) BZO-1400.

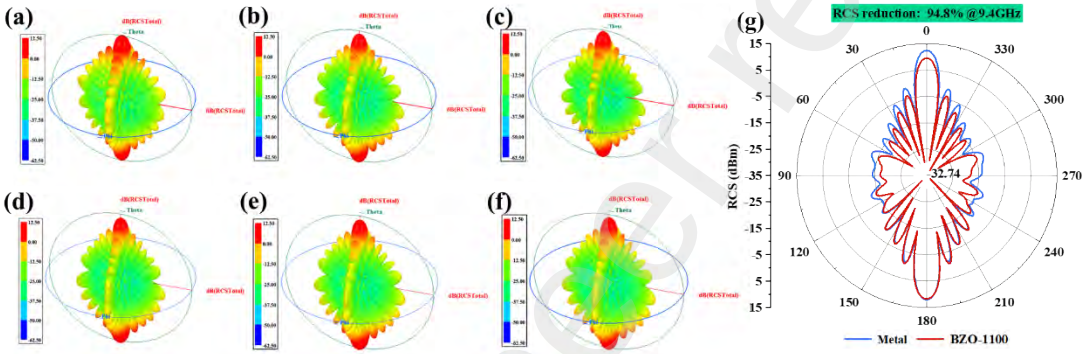

Fig. 11 Simulated results of RCS for (a) Metal, (b–f) BZO high-entropy ceramics, and (g) Comparison of RCS performance between metal and BZO-1100 specimens.

4. Conclusion

In this study, a series of $Ba(Zn_{0.2}Yb_{0.2}Ta_{0.2}Nb_{0.2}V_{0.2})O_3$ (BZO) high-entropy perovskite ceramics at different temperatures was successfully prepared by a simple high-temperature solid-phase method to obtain excellent EWA characteristics. Compared with other BZO specimens, BZO-1100 exhibits excellent EWA performance with an RL_{min} of −54.09 dB and an EAB of 2.81 GHz. The improved EWA performance is attributed to its excellent impedance matching as well as superior loss capability. The simulation of electric field distribution verifies that BZO-1100 shows better loss capability. The simulation of RCS proves that BZO-1100 exhibits potential for practical application. This study provides a significantly

important reference for the design of high-performance EWA materials and preparation of high-entropy perovskite ceramics with high EWA performance.

Acknowledgment

This study is supported by the Natural Science Foundation of Hunan Province (No. 2022JJ50086 and 2023JJ50182).

Data availability

Data will be made available on request.

References

[1] Guo YQ, Ruan KP, Wang GS, *et al.* Advances and mechanisms in polymer composites toward thermal conduction and electromagnetic wave absorption. *Sci Bull* 2023, **68**: 1195-1212.

[2] Yang BT, Fang JF, Xu CY, *et al.* One-Dimensional Magnetic FeCoNi Alloy Toward Low-Frequency Electromagnetic Wave Absorption. *Nano-Micro Lett* 2022, **14**: 170.

[3] Wu LP, Gao H, Guo RH, *et al.* MnO_2 Intercalation-Guided impedance tuning of Carbon/Polypyrrole double conductive layers for electromagnetic wave absorption. *Chem Eng J* 2023, **460**: 141749.

[4] Bi YX, Ma ML, Liao ZJ, *et al.* One-dimensional Ni@Co/C@PPy composites for superior electromagnetic wave absorption. *J Colloid Interface Sci* 2022, **605**: 483-492.

[5] Meng XW, Qiao J, Zheng SA, *et al.* Ternary Nickel/Molybdenum Dioxide/Carbon composited nanofibers for broadband and strong electromagnetic wave absorption. *Chem Eng J* 2023, **457**: 141241.

[6] Huang XM, Liu XH, Jia ZR, *et al.* Synthesis of 3D cerium oxide/porous carbon for enhanced electromagnetic wave absorption performance. *Adv Compos Hybrid Mater* 2021, **4**: 1398-1412.

[7] Wu ZC, Cheng HW, Jin C, *et al.* Dimensional Design and Core-Shell Engineering of Nanomaterials for Electromagnetic Wave Absorption. *Adv Mater* 2022, **34**: 2107538.

[8] Wang H, Zhao JR, Wang Z, *et al.* Bird-Nest-Like Multi-Interfacial MXene@SiC_{NWs}@Co/C Hybrids with Enhanced Electromagnetic Wave Absorption. *Acs Appl Mater Inter* 2023, **15**: 4580-4590.

[9] Zhang M, Zhao LB, Zhao WX, *et al.* Boosted electromagnetic wave absorption performance from synergistic induced polarization of SiC_{NWS}@MnO_2@PPy heterostructures. *Nano Research* 2023, **16**: 3558-3569.

[10] Zhang WM, Zhao B, Xiang HM, *et al.* One-step synthesis and electromagnetic absorption properties of high entropy rare earth hexaborides (HE REB_6) and high entropy rare earth

hexaborides/borates (HE REB_6/HE $REBO_3$) composite powders. *J Adv Ceram* 2021, **10**: 62-77.

[11] Li DS, Horikawa T, Liu JR, *et al.* Electromagnetic wave absorption properties of iron/rare earth oxide composites dispersed by amorphous carbon powder. *J Alloys Compd* 2006, **408**: 1429-1433.

[12] Zhu HH, Qin G, Zhou W, *et al.* Constructing flake-like ternary rare earth $Pr_3Si_2C_2$ ceramic on SiC whiskers to enhance electromagnetic wave absorption properties. *Ceram Int* 2024, **50**: 134-142.

[13] Yang YA, Xia L, Zhang T, *et al.* Fe_3O_4@LAS/RGO composites with a multiple transmission-absorption mechanism and enhanced electromagnetic wave absorption performance. *Chem Eng J* 2018, **352**: 510-518.

[14] Gao ZG, Jia ZR, Wang KK, *et al.* Simultaneous enhancement of recoverable energy density and efficiency of lead-free relaxor-ferroelectric BNT-based ceramics. *Chem Eng J* 2020, **402**: 125951.

[15] Idrees M, Batool S, Kong J, *et al.* Polyborosilazane derived ceramics - Nitrogen sulfur dual doped graphene nanocomposite anode for enhanced lithium ion batteries. *Electrochim Acta* 2019, **296**: 925-937.

[16] Xu HL, Yin XW, Li XL, *et al.* Lightweight Ti_2CT_x MXene/Poly(vinyl alcohol) Composite Foams for Electromagnetic Wave Shielding with Absorption-Dominated Feature. *Acs Appl Mater Inter* 2019, **11**: 10198-10207.

[17] Zhou XJ, Li SC, Zhang ML, *et al.* MXene/PEO aerogels with two-hierarchically porous architecture for electromagnetic wave absorption. *Carbon* 2023, **204**: 538-546.

[18] Jia ZR, Zhang XY, Gu Z, *et al.* MOF-derived Ni-Co bimetal/porous carbon composites as electromagnetic wave absorber. *Adv Compos Hybrid Mater* 2023, **6**.

[19] Shan Z, Cheng SY, Wu F, *et al.* Electrically conductive Two-dimensional Metal-Organic frameworks for superior electromagnetic wave absorption. *Chem Eng J* 2022, **446**: 137409.

[20] Yu LY, Zhu QQ, Guo ZQ, *et al.* Unique electromagnetic wave absorber for three-dimensional framework engineering with copious heterostructures. *J Mater Sci Technol* 2024, **170**: 129-139.

[21] Cheng SY, Pan XH, Xie AM, *et al.* Tuning electromagnetic absorption properties of transition metal oxides by hydrogenation with nascent hydrogen. *Chem Eng J* 2021, **417**: 127980.

[22] Wang CX, Wang BB, Cao X, *et al.* 3D flower-like Co-based oxide composites with excellent wideband electromagnetic microwave absorption. *Compos Pt B-Eng* 2021, **205**: 108529.

[23] Zhang WM, Dai FZ, Xiang HM, *et al.* Enabling highly efficient and broadband electromagnetic wave absorption by tuning impedance match in high-entropy transition metal diborides (HE TMB_2). *J Adv Ceram* 2021, **10**: 1299-1316.

[24] Yan ZK, Li DP, Zhang X, *et al.* Dual-phase high-entropy (FeCoNiZn)xV_2Oy oxides with promising microwave absorption properties. *Ceram Int* 2022, **48**: 36871-36879.

[25] Xiang HM, Xing Y, Dai FZ, *et al.* High-entropy ceramics: Present status, challenges, and a look forward. *J Adv Ceram* 2021, **10**: 385-441.

[26] Rost CM, Sachet E, Borman T, *et al.* Entropy-stabilized oxides. *Nature Communications* 2015, **6**: 8485.

[27] Li F, Zhou L, Liu J-X, *et al.* High-entropy pyrochlores with low thermal conductivity for thermal barrier coating materials. *J Adv Ceram* 2019, **8**: 576-582.

[28] Fu HX, Li S, Lin YC, *et al.* Enhancement of piezo-photocatalytic activity in perovskite $(Bi_{0.2}Na_{0.2}Ba_{0.2}K_{0.2}La_{0.2})TiO_3$ oxides via high entropy induced lattice distortion and energy band reconfiguration. *Ceram Int* 2024, **50**: 9159-9168.

[29] Jia YG, Chen SJ, Shao X, *et al.* Synergetic effect of lattice distortion and oxygen vacancies on high-rate lithium-ion storage in high-entropy perovskite oxides. *J Adv Ceram* 2023, **12**: 1214-1227.

[30] Li F, Cui W, Shao Y, *et al.* Preparing high-entropy ceramic films from high-entropy alloy substrate. *Mater Chem Phys* 2022, **287**: 126365.

[31] Du B, Liu YR, Xu JY, *et al.* Fabrication and electromagnetic wave absorbing properties of the $(Hf_{0.25}Zr_{0.25}Nb_{0.25}Ta_{0.25})C$ high-entropy ceramics. *J Alloys Compd* 2023, **969**: 172403.

[32] Xing Y, Dan WQ, Fan YC, *et al.* Low temperature synthesis of high-entropy $(Y_{0.2}Yb_{0.2}Sm_{0.2}Eu_{0.2}Er_{0.2})_2O_3$ nanofibers by a novel electrospinning method. *J Mater Sci Technol* 2022, **103**: 215-220.

[33] Zhang WM, Xiang HM, Dai FZ, *et al.* Achieving ultra-broadband electromagnetic wave absorption in high-entropy transition metal carbides (HE TMCs). *J Adv Ceram* 2022, **11**: 545-555.

[34] Ma JB, Zhao B, Xiang HM, *et al.* High-entropy spinel ferrites MFe_2O_4 (M = Mg, Mn, Fe, Co, Ni, Cu, Zn) with tunable electromagnetic properties and strong microwave absorption. *J Adv Ceram* 2022, **11**: 754-768.

[35] Zhang SJ, Jia ZR, Cheng B, *et al.* Recent progress of perovskite oxides and their hybrids for electromagnetic wave absorption: a mini-review. *Adv Compos Hybrid Mater* 2022, **5**: 2440-2460.

[36] Sunarso J, Hashim SS, Zhu N, *et al.* Perovskite oxides applications in high temperature oxygen separation, solid oxide fuel cell and membrane reactor: A review. *Prog Energy Combust Sci* 2017, **61**: 57-77.

[37] Akrami S, Edalati P, Fuji M, *et al.* High-entropy ceramics: Review of principles, production and applications. *Materials Science & Engineering R-reports* 2021, **146**: 100644.

[38] Cao MS, Wang XX, Zhang M, *et al.* Electromagnetic Response and Energy Conversion for Functions and Devices in Low-Dimensional Materials. *Adv Funct Mater* 2019, **29**: 1807398.

[39] Lv HL, Yang ZH, Pan HG, *et al.* Electromagnetic absorption materials: Current progress and new frontiers. *Prog Mater Sci* 2022, **127**: 100946.

[40] Mu Y, Ding D, Xiao G, *et al.* Molten-salt-assisted combustion synthesis of B_4C powders with high specific area and their electromagnetic wave absorbing performance. *Ceram Int* 2022, **48**: 34234-34242.

[41] Sun Y, Zhong W, Wang YQ, *et al.* MoS_2-Based Mixed-Dimensional van der Waals Heterostructures: A New Platform for Excellent and Controllable Microwave-Absorption Performance. *Acs Appl Mater Inter* 2017, **9**: 34243-34255.

[42] Xu WM, Li SB, Hu SJ, *et al.* Effect of Ti_3AlC_2 precursor and processing conditions on microwave absorption performance of resultant $Ti_3C_2T_x$ MXene. *J Mater Sci* 2021, **56**: 9287-9301.

[43] Zhang H, Liu H, Wu H, *et al.* Microwave absorbing property of gelcasting SiC-Si_3N_4 ceramics with hierarchical pore structures. *J Eur Ceram Soc* 2022, **42**: 1249-1257.

[44] Liu Y, Feng YR, Gong HY, *et al.* Electromagnetic wave absorption properties of nickel-containing polymer derived SiCN ceramics. *Ceram Int* 2018, **44**: 10945-10950.

[45] Geng TB, Yu GY, Shao GF, *et al.* Enhanced electromagnetic wave absorption properties of ZIF-67 modified polymer-derived SiCN ceramics by in situ construction of multiple heterointerfaces. *rare metals* 2023, **42**: 1635-1644.

[46] Mohammadabadi FH, Masoudpanah SM, Alamolhoda S, *et al.* Electromagnetic microwave absorption properties of high entropy spinel ferrite $((MnNiCuZn)_{1-x}Co_xFe_2O_4)$/graphene nanocomposites. *Journal of Materials Research and Technology-JMR&T* 2021, **14**: 1099-1111.

[47] Qian K, Yao Z, Lin H, *et al.* The influence of Nd substitution in Ni–Zn ferrites for the improved microwave absorption properties. *Ceram Int* 2020, **46**: 227-235.

[48] Zhang J, Wang W, Zhang Z, *et al.* Synthesis, microstructure and electromagnetic wave absorption properties of high-entropy carbide powders. *J Alloys Compd* 2023, **966**: 171593.

[49] Song LM, Zhang F, Chen YQ, *et al.* Multifunctional $SiC@SiO_2$ Nanofiber Aerogel with Ultrabroadband Electromagnetic Wave Absorption. *Nano-Micro Lett* 2022, **14**: 152.

[50] Zhang X, Qiao J, Jiang YY, *et al.* Carbon-Based MOF Derivatives: Emerging Efficient Electromagnetic Wave Absorption Agents. *Nano-Micro Lett* 2021, **13**: 135.

[51] Qiao L, Bi J, Yang Y, *et al.* In-situ synthesis of multi-principal-element $(Mo_{0.25}Cr_{0.25}Ti_{0.25}V_{0.25})_3C_2T_x$ MXene-based composites with enhanced electromagnetic wave absorption. *Ceram Int* 2023, **49**: 40498-40510.

[52] Wang W, Sun G, Sun X, *et al.* Electromagnetic wave absorbing properties of high-entropy transition metal carbides powders. *Mater Res Bull* 2023, **163**: 112212.

[53] Zhou W, Yin R-m, Long L, *et al.* SiC nanofibers modified Si_3N_4 ceramics for improved electromagnetic interference shielding in X-band. *Ceram Int* 2018, **44**: 2249-2254.

[54] Zhang XC, Liu MJ, Xu J, *et al.* Flexible and waterproof nitrogen-doped carbon nanotube arrays on cotton-derived carbon fiber for electromagnetic wave absorption and electric-thermal conversion. *Chem Eng J* 2022, **433**: 133794.

[55] Ma YZ, Pan AF, Yang XF, *et al.* Molten salt synthesis of highly crystalized (TaNbTiV)C flake and its electromagnetic wave absorption property. *Ceram Int* 2024, **50**: 81-93.

[56] Hou S, Wang Y, Gao F, *et al.* A novel approach to electromagnetic wave absorbing material design: Utilizing nano-antenna arrays for efficient electromagnetic wave capture. *Chem Eng J* 2023, **471**: 144779.